Title:

Detection of endogenous iron deposits in the injured mouse spinal cord through high-resolution *ex vivo* and *in vivo* MRI

Authors:

Linda V. Blomster[a,b], Gary Cowin[c], Nyoman D. Kurniawan[c] and Marc J. Ruitenberg[a,d*]

[a] The University of Queensland, School of Biomedical Sciences, St Lucia QLD 4072, Australia

[b] School of Anatomy and Human Biology, The University of Western Australia, Crawley WA 6009, Australia

[c] The University of Queensland, Centre for Advanced Imaging, St Lucia QLD 4072, Australia

[d] The Queensland Brain Institute, The University of Queensland, St Lucia QLD 4072, Australia

[*] Corresponding author:

Marc J. Ruitenberg, PhD

The University of Queensland

School of Biomedical Sciences

St Lucia, QLD 4072

Australia

Email: m.ruitenberg@uq.edu.au

Phone (fax): +61 7 3346 7602 (3365 1766)

Abstract

The main aim of this study was to employ high-resolution magnetic resonance imaging (MRI) to investigate the spatiotemporal development of pathological features associated with contusive spinal cord injury (SCI) in mice. Experimental mice were subjected to either sham surgery or moderate contusive SCI. A 16.4T small animal MR system was then employed for non-destructive imaging of post-mortem, fixed spinal cord specimens at the sub-acute (7 days) and more chronic stages (28-35 days) post-injury. Routine histological techniques were used for subsequent investigation of the observed neuropathology at the microscopic level. The central core of the lesion appeared as a dark hypo-intense area on MR images at all time points investigated. Interestingly, small focal hypo-intense spots were observed spreading through the dorsal funiculi proximal and distal to site of impact, particularly in those areas known to be undergoing gliosis and Wallerian degeneration. Histological examination revealed these hypo-intense spots to be high in iron content as determined by Prussian blue staining. Quantitative image analysis confirmed the increased presence of iron deposits at all post-injury time points investigated ($p<0.05$). Distant iron deposits were also detected via live imaging without the use of contrast-enhancing agents, enabling longitudinal investigation of this pathology in individual animals. Further immunohistochemical evaluation showed that intracellular iron co-localised to macrophages/microglia, astrocytes and oligodendrocytes in the sub-acute phase of SCI but predominantly $GFAP^{+}CC\text{-}1^{+}$ astrocytes at later stages of recovery. Thus, progressive, **w**idespread intraspinal iron accumulation is a feature of SCI in mice and high-resolution MRI can be effectively used as a diagnostic tool to monitor these neuropathological changes with time.

Keywords:

Neurotrauma, secondary injury, astrogliosis, neural scar, neurodegeneration, haemorrhage

Highlights:

- We used an ultra-high field (16.4T) MR system to image the lesioned mouse spinal cord.
- We then correlated abnormal features in MR images with microscopic histopathology.
- We show that hypo-intense MR features result from abnormal iron accumulation.
- Ultra-high field MRI was able to resolve this pathology at the single cell level.
- Intracellular iron stores could be visualised *ex vivo* as well as *in vivo*.

1. Introduction:

Spinal cord injuries (SCIs) typically involve a crush or bruising of the spinal cord as a result of fracture and/or dislocation of the spine, with most human cases classified as anatomically incomplete, contusive injuries (Bunge et al., 1993; Norenberg et al., 2004). Patients suffering SCI often experience symptoms that may include paralysis, loss of sensation and autonomic dysfunction at and below the level of injury (McDonald and Sadowsky, 2002); these disabilities are normally permanent because of the very limited inherent capacity of the mammalian central nervous system (CNS) to repair itself. The exact nature and severity of neurological impairments are heavily influenced by both the size and level of the injury (Ghasemlou et al., 2005; Lucin et al., 2007; Davis and Steward, 2010).

The initial mechanical damage inflicted on the spinal cord at the time of injury is traditionally defined as the 'primary injury'. This event triggers a complex series of pathophysiological cellular and molecular events in which oxidative stress, excitotoxicity and immune activation exacerbate the consequences of the primary injury by spreading the damage into the neighbouring neural tissue that was originally spared; these injurious cascades are collectively referred to as 'secondary damage' (for reviews, see Schwab and Bartholdi, 1996; Juurlink and Paterson, 1998; McDonald and Sadowsky, 2002). The ultimate appearance of the lesion site and associated neurological deficits are thus the resultant of both the primary and secondary injury.

Magnetic resonance imaging (MRI) is the most commonly used imaging modality to diagnose and study SCI in humans (Do-Dai et al., 2010; Cohen-Adad et al., 2011). The continuous improvements in MRI technology, including increasing magnetic field strengths, has increased resolution and improved soft tissue contrast, making it particularly well suited

to distinguish grey and white matter regions, and to detect subtle pathological changes in tissue structure and integrity within the lesioned spinal cord. High field MRI also enhances the detection of susceptibility effects from iron beyond the actual physical size of the deposit. With a number of putative therapeutics currently being tested for clinical use (for review, see Gensel et al., 2011), there is an urgent need to further develop and optimise non-invasive imaging methods to better study and characterise pathology in translational animal models of SCI.

The common pathology associated with human SCI can be accurately mimicked in rodent models of contusive injury (e.g. Scheff et al., 2004), and several studies have already utilised MRI to investigate lesion sites both *in vivo* and *ex vivo* albeit at inferior resolution (e.g. Nishi et al., 2007; Gonzalez-Lara et al., 2009; Gonzalez-Lara et al., 2010; Herrera et al., 2010; Byrnes et al., 2010; Gonzalez-Lara et al., 2011). The application of MRI to pre-clinical, animal-based SCI research offers several advantages, perhaps of greatest importance being the fact that MR imaging ultimately allows for longitudinal studies on lesion site development within live animals and direct translation to human trials because of its non-invasive nature. The development of more clinically relevant assessment methods to investigate important outcome parameters such as lesion volume, white matter sparing and treatment effects should ultimately aid the successful translation of putative therapeutics from bench-to-bedside.

The main aims of this study were to employ high-resolution MRI to investigate abnormal features associated with contusive SCI at unsurpassed resolution in both post-mortem tissue samples as well as live mice using a 16.4T small animal MRI, and to correlate abnormalities with microscopic pathology in tissue sections using conventional histological techniques and

immunostaining procedures. We demonstrate that ultra-high field MRI can be used to study the injured rodent spinal cord in great detail with no detectable loss of tissue antigenicity. Specifically, we report widespread iron accumulation not only within the lesion core but also more distant areas, particularly within the dorsal funiculus of the spinal cord, as part of normal SCI pathology. These trends could be observed both *ex vi*vo and with live imaging. Histological analysis confirmed the presence of small iron deposits outside the lesion core area, further revealing that these were mostly confined to reactive astrocytes. The established baseline data demonstrate the power of ultra-high field MRI as a diagnostic tool to detect pathological features at single cell resolution in SCI research.

2. Materials and methods:

2.1 Animals

Female C57BL6/J mice, 10-16 weeks of age, were housed under conventional conditions with a 12 hour light-dark cycle and free access to food and water. All experiments were approved by the The University of Queensland animal ethics committee and conducted in accordance with the policies established by the National Health and Medical Research Council (NHMRC), Australia. Mice were randomly allocated into the following groups: *(1)* SHAM-operated animals, i.e. "laminectomy only" (*n*=3), *(2)* 7 days post-SCI (*n*=4) and *(3)* 28-35 days post-SCI (*n*=5). After establishing MRI methodology *ex vivo,* longitudinal live imaging was conducted at day 0, 14 and 35 post-SCI (*n*=2). Of note, $Cx_3cr1^{+/gfp}$ mice were utilized (*n*=8 evenly spread over the groups) to aid the visualisation of activated microglia and blood borne macrophages at the injury site. In these mice, the coding sequence for enhanced green fluorescent protein (eGFP) was inserted into the Cx_3cr1 coding region, which places eGFP expression under Cx_3cr1 promoter control in the targeted allele (Jung et al., 2000).

2.2 Experimental spinal cord injury

Mice were anaesthetized with a mix of ketamine (10 mg/kg) and xylazil (20 mg/kg), following which a dorsal incision was made along the midline of the lower thoracic region. Next, the underlying paravertebral muscles were carefully split and dorsal laminectomy performed at the level of the thoracic (T) vertebra T9 to expose the underlying spinal cord. The vertebral column was then stabilized via rostral and caudal placement of Addson microforceps clamps, after which the mice were subjected to a moderate (50kdyne) force-controlled spinal contusion injury using the Infinite Horizon Impactor (Precision Systems and

Instrumentation, LLC). Following the impact, the muscles were stitched back together and the overlying skin sutured with Michel wound clips and/or Vetbond™ (3M Animal Care Products). Immediately after surgery, experimental mice received a single dose of buprenorphine (0.05 mg/kg), diluted in 1 ml of Hartmann's solution, in addition to administration of gentamycin (1 mg/kg) once daily for 5 days post-surgery. Bladders were voided manually twice daily for the duration of the experiment if required or until the return of the micturition reflex, whichever occurred first.

2.3 Tissue preparation for post-mortem imaging

Experimental mice were deeply anaesthetised with Lethabarb (150 mg/kg; Virbac, Australia) at the designated time point of 7 or 28-35 days post-SCI. Mice were then transcardially perfused with 20ml of heparinized saline (0.9% NaCl), followed by 30 ml of 4% paraformaldehyde (PFA) in phosphate-buffered saline (PBS: 1.7 mM NaH_2PO_4, 9 mM Na_2HPO_4, 0.15M NaCl, pH 7.4). The vertebral column was then dissected and post-fixed overnight at 4°C. After extensive washing in PBS, fixed specimens were subsequently incubated in PBS containing 0.2% (v/v) of the contrast-enhancing agent Magnevist® (Bayer, Australia) for >24 hours pre-imaging.

2.4 Post-mortem magnetic resonance (MR) imaging

All MRI data was acquired at the Centre for Advanced Imaging (The University of Queensland) using a 16.4T vertical wide-bore NMR spectrometer, interfaced with Advance II electronics, running Paravision 5.0 software (Bruker BioSpin, Germany) Fixed specimens of the lower thoracic vertebral column and spinal cord were trimmed such that they fitted tightly into a 1.0 cm glass tube whilst still immersed in Magnevist/PBS solution. The tube was then placed inside a quadrature birdcage coil with an inner diameter of 10 mm (M2M Imaging

Inc., USA). T_1/T_2^*-weighted images were acquired using a 3D gradient echo FLASH sequence (Fast Low Angle Shot; Haase et al., 1986). Gradient-echo sequence was chosen as the preferred MRI acquisition sequence because it can produce ultra-high resolution images with greater signal-to-noise per unit time. Furthermore, at high magnetic field, the gradient echo sequence is also highly sensitive to local magnetic-field inhomogeneity such as small paramagnetic iron deposits in tissues. Specific imaging parameters were as follows: TR/TE=40/6.5 ms, flip angle = Ernst angle ~ 25°, field-of-view = 8X28X8 mm, acquisition matrix 400X1024X400, image resolution 20X27X20 µm, averages = 4, acquisition time = 12 hrs 40 min. These imaging parameters were settled upon after pilot studies revealed that shorter 'Echo Times' (TEs) provided clear visualization of the hypointense regions of the injured spinal cord while still maintaining adequate contrast between grey and white matter (Fig. 1). MR images were viewed and processed using OsiriX imaging software (Pixmeo SARL, Geneva, Switzerland; Rosset et al., 2004).

2.5 Tissue processing for histological analysis

Following the conclusion of post-mortem MR imaging, the spinal cords were dissected out from the vertebral columns and washed extensively in PBS. Next, the tissue was cryoprotected via subsequent overnight incubations in PBS containing 10% and 30% sucrose, respectively. Spinal cords were then snap-frozen in dry ice-cooled iso-pentane and stored at -80^{o}C until further processing. Tissue sections (16µm) were cut on a Leica cryostat and collected in 1:5 series on Superfrost Plus slides (Menzel, Germany). Slides were air-dried for 2 hours and then stored at -80^{o}C until further processing.

2.6 Prussian Blue staining and immunohistochemical staining procedures

Standard Prussian blue staining was used to visualise iron accumulation within the tissue. In brief, slides were allowed to air dry before being washed in distilled water for 3 x 5 min. Slides were then incubated in 10% ferrocyanide solution (w/v; Sigma) for 10 min at room temperature (RT), followed by a 15 min incubation in 5% ferrocyanide (w/v) + 5% HCl solution (v/v). After development of the staining, slides were washed for 3 x 5 min with distilled water. Slides were then dehydrated in gradients of ethanol and cleared with xylene before being coversliped with DPX mounting medium (Merck Pty. Ltd., Australia).

When combined with immunohistochemistry, slides were washed 3 x 5 min in PBS following the conclusion of Prussian blue staining (as detailed above), followed by quenching of endogenous peroxidise activity with 0.3% H_2O_2 in 100% methanol for 20 min. After another round of washings, slides were immersed in blocking solution containing 2% Bovine Serum Albumin (BSA; Sigma) and 0.2% Triton X-100 (Sigma) in PBS for 1 hour to reduce non-specific antibody binding. BEAT^{TM} blocker kit (Invitrogen) was employed according to manufacturer's instructions where appropriate to allow for the use of mouse primary antibodies on mouse tissue. The sections were incubated overnight in a humidified chamber at 4^{o}C with either primary rabbit anti-GFP antibody (1:800; Millipore), rabbit anti-GFAP (1:1000; DakoCytomation) or mouse anti-CC1 (1:500; Abcam). The following day, slides were washed extensively for 3 x 10 min in PBS and incubated with the appropriate secondary antibody, i.e. biotinylated goat anti-rabbit or horse anti-mouse antibody (1:200; Vector Laboratories) for 1.5 hours at RT. After another round of washings to remove unbound antibody, slides were incubated with ABC reagent (1:200; Vector laboratories) for 1 hour at RT. The staining was developed after a final round of washings by incubating the slides for approximately 6 min with either 3, 3-diaminobenzidine (DAB; Sigma) or 3-amino-9-ethylcarbazole (EAC; Sigma), resulting in a brown or red precipitate, respectively. The

reaction was stopped via immersion of the slides in ddH_2O, after which they were dehydrated through graded series of ethanol (DAB staining) and coverlipped in DPX mounting medium. For AEC staining, sections were covered with ImmunoHistoMount (Sigma) and air dried for approximately one day before being coverslipped in DPX mounting medium.

2.7 Quantification of Prussian blue staining

Prussian blue stained tissue sections were scanned on an Aperio scanscope system using the 20x objective. For each animal, three sections, both rostral and caudal from the injury site, covering ~3-5 mm in each direction, were randomly chosen for iron quantification. Matching sections were selected from SHAM-operated control animals. The relative area of the section covered by Prussian blue staining was calculated in ImageJ by dividing the positively stained, i.e. iron-containing areas by the total area of each section. Since no differences were observed between measures taken from proximal or distal segments of the spinal cord, the percentage area obtained for each section was averaged for each animal (i.e. 6 sections in total per animal).

2.8 In vivo MR imaging

In vivo MR imaging was performed to determine if iron accumulation could be detected within the injured spinal cord of live mice. For this, mice were anaesthetized using 1.5-2% isoflurane and oxygen as a diluent (1 L/min). A 1.5x3 cm transmit/receive linear surface coil (M2M Imaging) was placed dorsally over the injured area of the spinal cord. Breathing was monitored throughout the duration of imaging using BIOTRIG (SpinSystems, Australia) and maintained around 40 breaths per minute by adjusting the isoflurane level and oxygen flow rate as appropriate. Respiratory gating was employed to reduce movement artifacts. Gradient echo 2D images were acquired using the following parameters: TR = 350ms, TE = 2.83 ms,

flip angle=40^{o}, slice thickness = 250 µm, number of slices = 11, field-of-view = 40X10mm, matrix = 320X128, image resolution 125X78 µm, averages = 12, acquisition time = 7.5 min. Spin echo based RARE images were also acquired with the same geometry and the following parameters, TE = 14 ms, RARE factor = 4, TR = 1000, averages = 12, acquisition time = 6.5 min.

2.9 Statistical analysis

Obtained datasets were analyzed for differences in levels of intra-spinal iron using one-way ANOVA and Newman-Keuls post-hoc test. Data sets were considered to be significantly different from each other if a p-value of less than 0.05 was obtained.

3. Results:

3.1 Hypo-intense regions are a pathological feature in T_1/T_2^* MR images of the injured mouse spinal cord

Post-mortem, high-resolution MRI was conducted using a 16.4T small animal MRI in the sub-acute and more chronic stages of spinal cord injury, i.e. 7 and 28-35 days post-injury, respectively, as well as for sham-operated mice. In all MR images of the injured spinal cord with scar development, the central core of the lesion appeared as a dark hypo-intense area (Fig. 2A, C). Discrete points of loss of MR signal were also apperent further away from the lesion site, mostly along the dorsal funiculi (arrows in A and C). This loss of signal was very prominent at 7 days post-injury both proximal and caudal to the injury site (Fig. 2A), where it was detected for at least up to 3.5 ± 0.5mm and 4.8 ± 1.0mm, respectively. Signal loss along the dorsal columns was still apparent as time progressed to the more cronic stages (Fig. 2C), both rostrally (4.1 ± 1.1mm) as well as caudally (2.5 ± 0.8mm) from the lesion epicentre. SHAM-operated animals did not show any such hypo-intense regions within the spinal cord (Fig. 2D).

3.2. Prussian Blue staining correlates MRI hypointense regions with iron deposition

MR images were next compared to Prussian blue stains of the same specimens in order to determine whether the loss of MR signal following SCI resulted from iron accumulation. Prussian blue staining revealed a uniform and diffuse iron presence throughout the lesion core (Fig. 2B). A more distinct and scattered iron staining pattern, which appeared to be intracellular, was present in the grey and white matter areas surrounding the lesion core. Further distal and proximal to the lesion site, Prussian blue staining was mostly localised to the dorsal column area, in a fashion that appeared to largely overlap with the observed

distribution of hypo-intense regions in MR images. Coronal sectioning confirmed the presence of Prussian blue^{+} cell-shaped structures in the dorsal column area, both proximal (Fig. 2E) and distal (Fig. 2F) to the lesion core of experimental mice at 28-35 days post-SCI. Iron accumulation was evident in tissue sections for at least 5 millimetres proximal and distal to the lesion site, i.e. the furthest point investigated. Quantitative analysis of Prussian blue content in these areas revealed significantly higher ($p<0.05$) iron accumulation rostral and caudal to the lesion site at both 7 and 28-35 days post-injury in comparison to sham-operated mice (Fig. 2G).

3.3 Iron accumulation following SCI is mostly confined to the lesion epicentre and reactive astrocytes

Double immunohistochemical staining procedures with glial- and macrophage-specific antibodies were used to further examine the distribution pattern of Prussian blue staining that was observed in the injured spinal cord relative to hypo-intense areas within MR images. Examination of a higher power cross-sectional post-mortem MR image at 28 days post-injury again showed the lesion epicentre as a black, hypo-intense region with well defined lesion borders in addition to several other hypo-intense clusters at the lesion margins (Fig. 3A), while hyper-intense regions in the spared white matter around the central lesion core represent demyelinated areas (Cowin et al., 2011). A transverse histology section of the same specimen and at approximately the same location revealed a remarkable overlap between the hypo-intense regions in the MR image and Prussian blue stained regions (Fig. 3B). A more diffuse pattern of Prussian blue staining was present throughout the lesion core, most likely associated with deposition of extracellular matrix within the neural scar. More distinct iron deposits were found scattered around the lesion margins as well as in proximal and distal direction. These deposits appeared to be intracellular based on their morphological

appearance. We used *Cx$_3$cr1^{gfp}* mice on the assumption for this iron staining to be most likely present inside phagocytic macrophages, potentially as a result of coagulated blood clearance and associated debris from the injury site. However, little overlap was observed between GFP-stained macrophages and Prussion blue staining. Most of the activated microglia and/or macrophages in the injured spinal cord did not show any intracellular iron deposits and the few double-positive cells that were observed were mostly present at at the lesion margin (Fig. 3C, D). Additional double staining on adjacent sections revealed that most of this accumulated iron was present inside GFAP$^+$ astrocytes at the 28-35 day time point (Fig. 3E). Further examination of iron accumulation at the earlier time point, i.e. 7 days post-SCI, revealed again that most of this had accumulated inside GFAP$^+$ astrocytes (Fig. 4A-C) although slightly more Prussian blue$^+$ macrophages/microglia (Fig. 4D-E) were qualitatively observed at this early timepoint. As oligodendrocyes in the injured spinal cord are also known to contain high levels of iron (Schonberg and McTigue, 2009), we conducted additional stainings using CC-1 as a marker for mature oligodendrocytes. Indeed, CC-1$^+$ cells with typical oligodendrocyte morphology and intracellular iron stores could be detected around the lesion center as well as more proximal and distal to it at the early 7 day time point (Fig. 4G-I).

3.4 Visualising iron accumulation within the injured spinal cord of live mice

We next sought to ascertain that the above detailed MR features associated with SCI pathology could also be detected through live-imaging with much shorter imaging times and without pre-treatment with Magnevist® for contrast enhancement. For *in vivo* MRI, we made use of the 3D gradient-echo imaging protocol that was developed for post-mortem tissue samples, with the parameters being adjusted for 2D image acquisition to shorten sampling

time, a longer TR to compensate for the absence of Magnevist contrast agent, and a shorter TE to minimize imaging artifacts from bone. Spin echo images of the same sample were also collected. Regardless of acquisition method, the lesion core already shows up as a dark hypo-intense region immediately after SCI (i.e. 4 hours post-injury; Fig. 5A), which is most likely the result of microhaemorrhaging caused upon impact by the actual contusion injury of the spinal cord. Importantly, no hypo-intense spots were observed in areas more distant to the lesion site at this very early time point post-injury. However, at 2 weeks post-injury, hypo-intense signals had now developed within these regions and were clearly visible along the caudal axis (Fig. 5B). By 35 days post-injury, hypo-intense areas on MR images could be detected at even greater distances away from the original site of impact (Fig. 5C), indicating that they are a feature of secondary pathology following SCI and emerge over time. Distant hypo-intense areas within MR images appeared to be mostly located within or near the dorsal column area. Development of a cystic cavity, which occurred between day 14 and day 35, became apparent as bright white, hyper-intense region at the lesion epicenter (Fig. 5C, D). High-resolution, post-mortem imaging of the same specimen at 35 days post-injury confirmed the existence of distant hypo-intense areas within the spinal cord as well as the presence of a cystic cavity at the original impact site (Fig. 5D).

4. Discussion:

High-resolution MRI is increasingly finding its way into murine models of neurological disease, including SCI. MRI has already been used as a tool to measure lesion volume (Nishi et al., 2007), white matter sparing and degeneration through diffusion-weighted imaging (Kozlowski et al., 2008; Ellingson et al., 2008; Ellingson et al., 2010) and inflammatory changes (Ahrens et al., 2011). Our data demonstrate that conventional MRI can still reveal subtle pathological features as a result of SCI in and around the lesion site as well as further proximal and distal to the site of impact, which may have otherwise gone unnoticed in routine histological examination. Specifically, we found in both live mice and post-mortem tissue samples that both lesion core and more distant regions contained dark hypo-intense areas in gradient echo T_2* weighted MR images as a result of high iron content, except for one relatively rare occasion in which cyst formation occurred at the impact site (Fig 5C and D). Similar hypo-intense signals at the primary injury site have been previously reported upon in spinal cord-injured rodents (e.g. Gonzalez-Lara et al., 2009; Qian et al., 2010; Gonzalez-Lara et al., 2011) and humans (Wang et al., 2011), but not distal or proximal to the primary injury site as observed here.

The acute presence of iron at the lesion epicentre is most likely explained by the initial microhaemorrhaging that occurs as a result of blood-spinal cord barrier disruption following traumatic contusive injury (Bilgen and Rumboldt, 2008). As iron gets recycled in the CNS, it is usually stored within a complex known as hemosiderin. Iron accumulation and hemosiderin formation as part of normal SCI pathology is an occurring feature in both rodents (Liu et al., 2004; Rathore et al., 2008; Gonzalez-Lara et al., 2011) and humans (Koszyka et al., 2002). The ability to non-invasively detect and monitor iron content in the

CNS may have important implications as previous studies have shown that the formation and accumulation of hemosiderin can cause neuronal damage (Heye et al., 1994). In addition, removal of accumulated iron from the injured spinal cord with iron chelators reportedly improves the functional outcome through mechanisms that could involve reduced inflammation (Paterniti et al., 2010) and/or axonal regeneration (for review, see Brazda and Müller, 2009). As we were able to show that hypo-intense signals as a result of iron presence within the tissue could be easily detected without the use of any contrast enhancing agents, high-resolution MR imaging in live animals may provide an important advance by being able to monitor the efficacy of iron chelator treatment and lesion site development in pre-clinical and clinical studies.

The combination of non-destructive high-resolution MR imaging with subsequent histological analysis of the same sample allowed us to further examine the nature of any abnormal features that were observed. While the hypo-intense signals at the lesion epicentre nicely correlated with the more diffuse pattern of Prussian Blue staining within the tissue of the neural scar, iron accumulation in more distant regions was found to be mostly intracellular. Accumulation of intracellular iron in the injured spinal cord has been reported previously in both microglia/macrophages and oligodendrocytes through histological means (Rathore et al., 2008; Schonberg and McTigue, 2009). We confirmed the presence of intracellular iron in activated microglia/macrophages as well as oligodendrocytes and provide the first evidence that such intracellular iron stores can be detected with relative ease through high-resolution MRI in post-mortem tissue samples as well as live animals. Interestingly, however, the majority of more distant hypo-intense MR features appeared to arise from high levels of intracellular iron in $GFAP^+$ astrocytes. These cells displayed a reactive or hypertrophic appearance and were mostly located within the white matter of the dorsal

funiculus. Little is known about the role of astrocytes in iron metabolism following SCI but abnormal iron accumulation in astrocytes was previously reported in a rat model of demyelinating disease (Izawa et al., 2010). Although beyond the scope of the present study, it is tempting to speculate that such high levels of intracellular iron may be indicative of oxidative stress and an indicator of astrogliosis, particularly in those areas undergoing prominent Wallerian degeneration. It would be of interest to further investigate this in future studies, perhaps with a more severe injury that also engages the lateral funiculi.

Finally, supramagnetic iron particles are increasingly being used for labelling and vivo tracking of cell transplants through MRI technology, and numerous studies have already applied these in context of the spinal cord (e.g. Dunning et al., 2004; Dunning et al., 2006; Geffner et al., 2008; Hu et al., 2009; Gonzales-Laura et al., 2009; Gonzales-Laura et al., 2011). The present study indicates that, although the loss of MR signal (hypo-intensity) with supramagnetic particles is usually far greater than that observed as a result of endogenous iron stores, abnormal iron accumulation as a result of pathology should be appropriately controlled for, particularly when using ultra-high field MR systems and/or subsequent histological means to identify transplanted cells.

In conclusion, we have demonstrated that high-resolution MRI provides a useful tool to assess general SCI-related pathology and for monitoring lesion site development. We further show that the 16.4T small animal MR system provides enough power to visualize intracellular iron accumulation within populations of astrocytes, microglia/macrophages and oligodendrocytes in the injured mouse spinal cord.

References:

Ahrens, E.T., Young, W.B., Xu, H., Pusateri, L.K., 2011. Rapid quantification of inflammation in tissue samples using perfluorocarbon emulsion and fluorine-19 nuclear magnetic resonance. Biotechniques. 50**,** 229-34.

Bilgen, M., Rumboldt, Z., 2008. Neuronal and vascular biomarkers in syringomyelia: investigations using longitudinal MRI. Biomark Med. 2**,** 113-24.

Brazda, N., Muller, H.W., 2009. Pharmacological modification of the extracellular matrix to promote regeneration of the injured brain and spinal cord. Prog Brain Res. 175**,** 269-81.

Bunge, R.P., Puckett, W.R., Becerra, J.L., Marcillo, A., Quencer, R.M., 1993. Observations on the pathology of human spinal cord injury. A review and classification of 22 new cases with details from a case of chronic cord compression with extensive focal demyelination. Adv Neurol. 59**,** 75-89.

Byrnes, K.R., Fricke, S.T., Faden, A.I., 2010. Neuropathological differences between rats and mice after spinal cord injury. J Magn Reson Imaging. 32**,** 836-46.

Cohen-Adad, J., El Mendili, M.M., Lehericy, S., Pradat, P.F., Blancho, S., Rossignol, S., Benali, H., 2011. Demyelination and degeneration in the injured human spinal cord detected with diffusion and magnetization transfer MRI. Neuroimage 55, 1024-33.

Cowin, G.J., Butler, T.J., Kurniawan, N.D., Watson, C., Wallace, R.H., 2011. Magnetic resonance microimaging of the spinal cord in the SOD1 mouse model of amyotrophic lateral sclerosis detects motor nerve root degeneration. Neuroimage. 58**,** 69-74.

David, B.T., Steward, O., 2010. Deficits in bladder function following spinal cord injury vary depending on the level of the injury. Exp Neurol. 226**,** 128-35.

Do-Dai, D.D., Brooks, M.K., Goldkamp, A., Erbay, S., Bhadelia, R.A., 2010. Magnetic resonance imaging of intramedullary spinal cord lesions: a pictorial review. Curr Probl Diagn Radiol. 39**,** 160-85.

Dunning, M.D., Lakatos, A., Loizou, L., Kettunen, M., ffrench-Constant, C., Brindle, K.M., Franklin, R.J., 2004. Superparamagnetic iron oxide-labeled Schwann cells and olfactory ensheathing cells can be traced in vivo by magnetic resonance imaging and retain functional properties after transplantation into the CNS. J Neurosci. 24**,** 9799-810.

Dunning, M.D., Kettunen, M.I., Ffrench Constant, C., Franklin, R.J., Brindle, K.M., 2006. Magnetic resonance imaging of functional Schwann cell transplants labelled with magnetic microspheres. Neuroimage. 31**,** 172-80.

Ellingson, B.M., Ulmer, J.L., Kurpad, S.N., Schmit, B.D., 2008. Diffusion tensor MR imaging in chronic spinal cord injury. AJNR Am J Neuroradiol. 29**,** 1976-82.

Ellingson, B.M., Schmit, B.D., Kurpad, S.N., 2010. Lesion growth and degeneration patterns measured using diffusion tensor 9.4-T magnetic resonance imaging in rat spinal cord injury. J Neurosurg Spine. 13**,** 181-92.

Geffner, L.F., Santacruz, P., Izurieta, M., Flor, L., Maldonado, B., Auad, A.H., Montenegro, X., Gonzalez, R., Silva, F., 2008. Administration of autologous bone marrow stem cells into spinal cord injury patients via multiple routes is safe and improves their quality of life: comprehensive case studies. Cell Transplant. 17**,** 1277-93.

Gensel, J.C., Donnelly, D.J., Popovich, P.G., 2011. Spinal cord injury therapies in humans: an overview of current clinical trials and their potential effects on intrinsic CNS macrophages. Expert Opin Ther Targets. 15**,** 505-18.

Ghasemlou, N., Kerr, B.J., David, S., 2005. Tissue displacement and impact force are important contributors to outcome after spinal cord contusion injury. Exp Neurol. 196**,** 9-17.

Gonzalez-Lara, L.E., Xu, X., Hofstetrova, K., Pniak, A., Brown, A., Foster, P.J., 2009. In vivo magnetic resonance imaging of spinal cord injury in the mouse. J Neurotrauma. 26**,** 753-62.

Gonzalez-Lara, L.E., Xu, X., Hofstetrova, K., Pniak, A., Chen, Y., McFadden, C.D., Martinez-Santiesteban, F.M., Rutt, B.K., Brown, A., Foster, P.J., 2011. The use of cellular magnetic resonance imaging to track the fate of iron-labeled multipotent stromal cells after direct transplantation in a mouse model of spinal cord injury. Mol Imaging Biol. 13**,** 702-11.

Haase, A., Frahm, J., Matthaei, D., Hanicke, W., Merboldt, K.D., 1986. Flash Imaging - Rapid Nmr Imaging Using Low Flip-Angle Pulses. Journal of Magnetic Resonance. 67**,** 258-266.

Herrera, J.J., Sundberg, L.M., Zentilin, L., Giacca, M., Narayana, P.A., 2010. Sustained expression of vascular endothelial growth factor and angiopoietin-1 improves blood-spinal cord barrier integrity and functional recovery after spinal cord injury. J Neurotrauma. 27**,** 2067-76.

Heye, N., Kastrup, O., Terstegge, K., Faiss, J.H., Iglesias, J.R., 1994. Superficial siderosis of the central nervous system. Arch Gerontol Geriatr. 18**,** 181-90.

Hu, S.L., Zhang, J.Q., Hu, X., Hu, R., Luo, H.S., Li, F., Xia, Y.Z., Li, J.T., Lin, J.K., Zhu, G., Feng, H., 2009. In vitro labeling of human umbilical cord mesenchymal stem cells with superparamagnetic iron oxide nanoparticles. J Cell Biochem. 108**,** 529-35.

Izawa, T., Yamate, J., Franklin, R.J., Kuwamura, M., 2010. Abnormal iron accumulation is involved in the pathogenesis of the demyelinating dmy rat but not in the hypomyelinating mv rat. Brain Res. 1349**,** 105-14.

Jung, S., Aliberti, J., Graemmel, P., Sunshine, M.J., Kreutzberg, G.W., Sher, A., Littman, D.R., 2000. Analysis of fractalkine receptor CX(3)CR1 function by targeted deletion and green fluorescent protein reporter gene insertion. Mol Cell Biol. 20**,** 4106-14.

Juurlink, B.H., Paterson, P.G., 1998. Review of oxidative stress in brain and spinal cord injury: suggestions for pharmacological and nutritional management strategies. J Spinal Cord Med. 21**,** 309-34.

Koszyca, B., Manavis, J., Cornish, R.J., Blumbergs, P.C., 2002. Patterns of immunocytochemical staining for ferritin and transferrin in the human spinal cord following traumatic injury. J Clin Neurosci. 9**,** 298-301.

Kozlowski, P., Raj, D., Liu, J., Lam, C., Yung, A.C., Tetzlaff, W., 2008. Characterizing white matter damage in rat spinal cord with quantitative MRI and histology. J Neurotrauma. 25**,** 653-76.

Liu, J.B., Tang, T.S., Xiao, D.S., 2004. Changes of free iron contents and its correlation with lipid peroxidation after experimental spinal cord injury. Chin J Traumatol. 7**,** 229-32.

Lucin, K.M., Sanders, V.M., Jones, T.B., Malarkey, W.B., Popovich, P.G., 2007. Impaired antibody synthesis after spinal cord injury is level dependent and is due to sympathetic nervous system dysregulation. Exp Neurol. 207**,** 75-84.

McDonald, J.W., Sadowsky, C., 2002. Spinal-cord injury. Lancet. 359**,** 417-25.

Nishi, R.A., Liu, H., Chu, Y., Hamamura, M., Su, M.Y., Nalcioglu, O., Anderson, A.J., 2007. Behavioral, histological, and ex vivo magnetic resonance imaging assessment of graded contusion spinal cord injury in mice. J Neurotrauma. 24**,** 674-89.

Norenberg, M.D., Smith, J., Marcillo, A., 2004. The pathology of human spinal cord injury: defining the problems. J Neurotrauma. 21**,** 429-40.

Paterniti, I., Mazzon, E., Emanuela, E., Paola, R.D., Galuppo, M., Bramanti, P., Cuzzocrea, S., 2010. Modulation of inflammatory response after spinal cord trauma with deferoxamine, an iron chelator. Free Radic Res. 44**,** 694-709.

Qian, J., Herrera, J.J., Narayana, P.A., 2010. Neuronal and axonal degeneration in experimental spinal cord injury: in vivo proton magnetic resonance spectroscopy and histology. J Neurotrauma. 27**,** 599-610.

Rathore, K.I., Kerr, B.J., Redensek, A., Lopez-Vales, R., Jeong, S.Y., Ponka, P., David, S., 2008. Ceruloplasmin protects injured spinal cord from iron-mediated oxidative damage. J Neurosci. 28**,** 12736-47.

Rosset, A., Spadola, L., Ratib, O., 2004. OsiriX: an open-source software for navigating in multidimensional DICOM images. J Digit Imaging. 17**,** 205-16.

Scheff, S.W., Dhillon, H.S., 2004. Creatine-enhanced diet alters levels of lactate and free fatty acids after experimental brain injury. Neurochem Res. 29**,** 469-79.

Schonberg, D.L., McTigue, D.M., 2009. Iron is essential for oligodendrocyte genesis following intraspinal macrophage activation. Exp Neurol. 218**,** 64-74.

Schwab, M.E., Bartholdi, D., 1996. Degeneration and regeneration of axons in the lesioned spinal cord. Physiol Rev. 76**,** 319-70.

Wang, M., Dai, Y., Han, Y., Haacke, E.M., Dai, J., Shi, D., 2011. Susceptibility weighted imaging in detecting hemorrhage in acute cervical spinal cord injury. Magn Reson Imaging. 29**,** 365-73.

Figures:

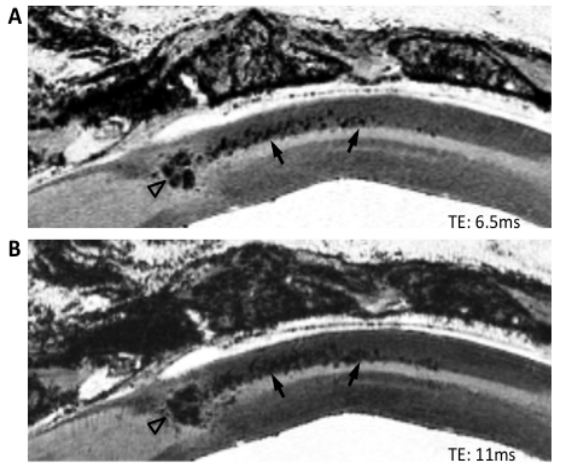

Figure 1. Post-mortem MR images of injured mouse spinal cord at 35 days post-SCI. Note that a shorter TE better illustrates structure within the hypo-intense core of the lesion (arrowheads, A *vs*. B). A longer TE did increase the contrast between grey and white matter regions, however, this came at the cost of diminished contrast between more distant hypo-intense features of interest and spinal cord white matter (arrows, A *vs*. B). Also note that a longer TE causes an increase in susceptibility artefacts around the bone, loss of trabecular bone definition and defined edges of the bone.

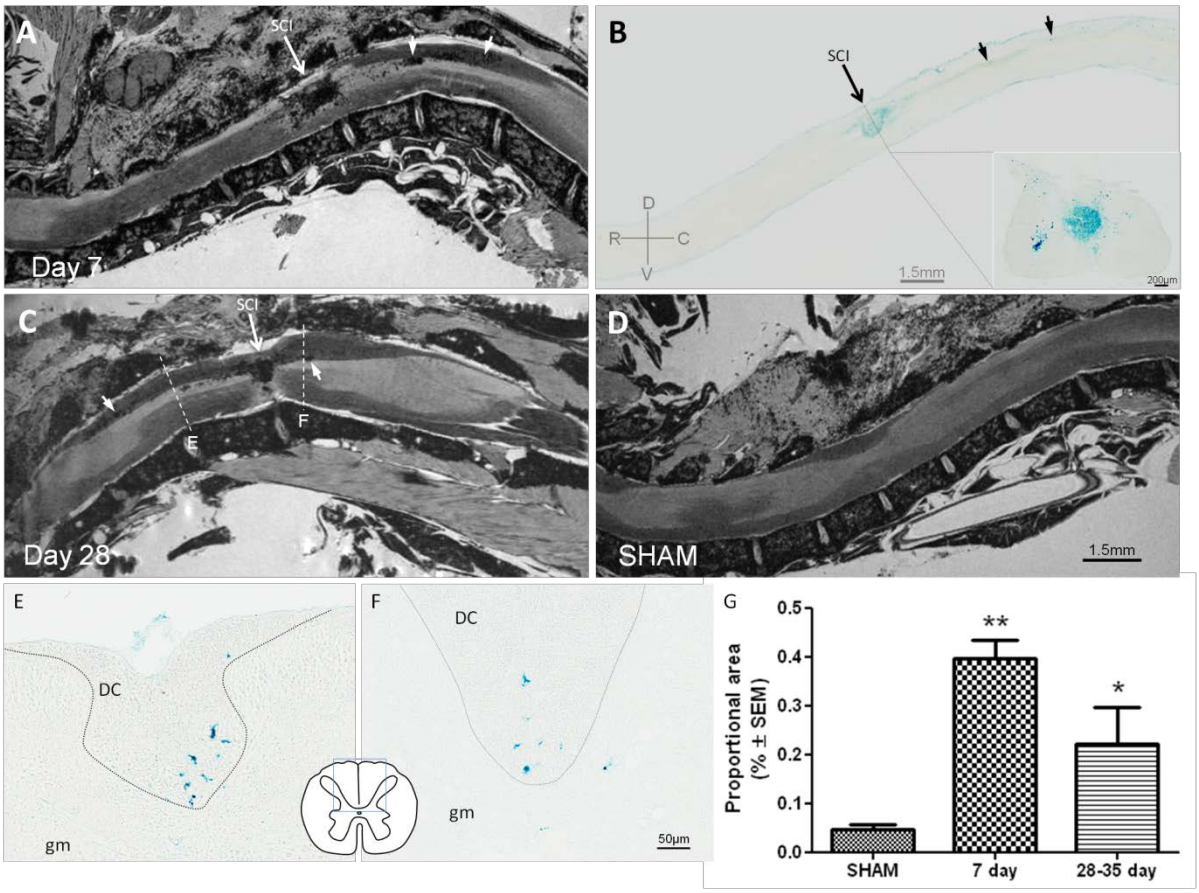

Figure 2. Post-mortem MR images of mouse spinal cord at (**A**) day 7 and (**C**) day 28 post-SCI. In the absence of cyst formation, the central core of the lesion appeared as a dark hypo-intense area. Additional loss of signal was observed spreading for at least several millimeters through the dorsal funiculi proximal and distal to site of impact (arrows in A and C), particularly in those areas undergoing substantial Wallerian degeneration. (**B**) Histological examination revealed these hypo-intense areas to be high in iron content as determined by Prussian blue staining. Inset shows a representative example of iron staining in a coronal section through the lesion epicenter. (**D**) No atypical MR signal was observed in SHAM operated mice. Abnormal levels of intracellular iron (blue) were observed (**E**) proximal and (**F**) distal to the lesion site, particularly within the dorsal column area. (**G**) Quantitative image analysis confirmed the presence of distant, abnormal iron levels within injured spinal cord at all time points ($p<0.05$).

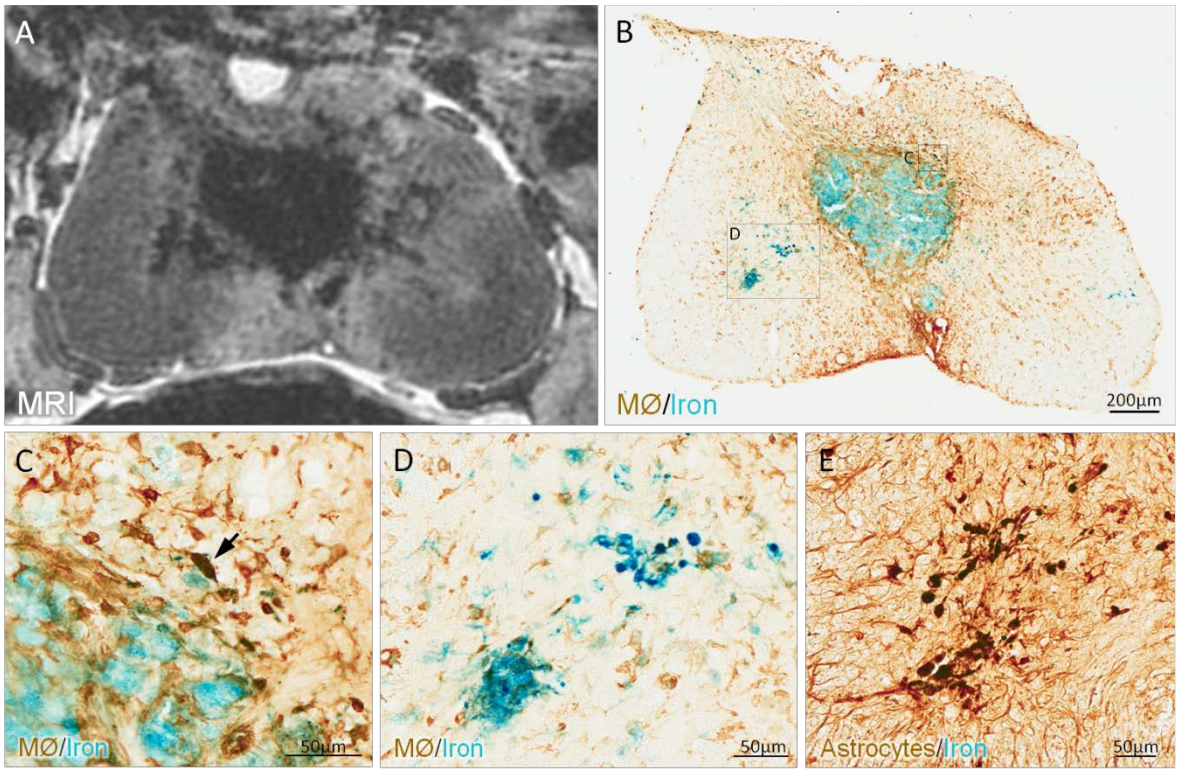

Figure 3. (**A**) Cross-sectional *ex vivo* MR image showing hypo-intense regions at the spinal cord lesion epicenter at 28 days post-injury. (**B**) Histological section taken from approximately the same area as shown in A, showing GFP-stained $Cx_3cr1^{gfp/+}$ macrophages (MØ) and iron. (**C**-**D**) Higher power pictures of boxed areas shown in B. Note that Prussian Blue stain at the lesion epicenter appears mostly diffuse and acellular (**C**). Only occasional co-localization of iron within GFP^+ macrophages was observed (C, arrow). (**E**) Adjacent section of B, showing the equivalent of the boxed area ´D´. Note the high incidence of co-localization between Prussian Blue stain and $GFAP^+$ astrocytes (blue + brown => dark green / black).

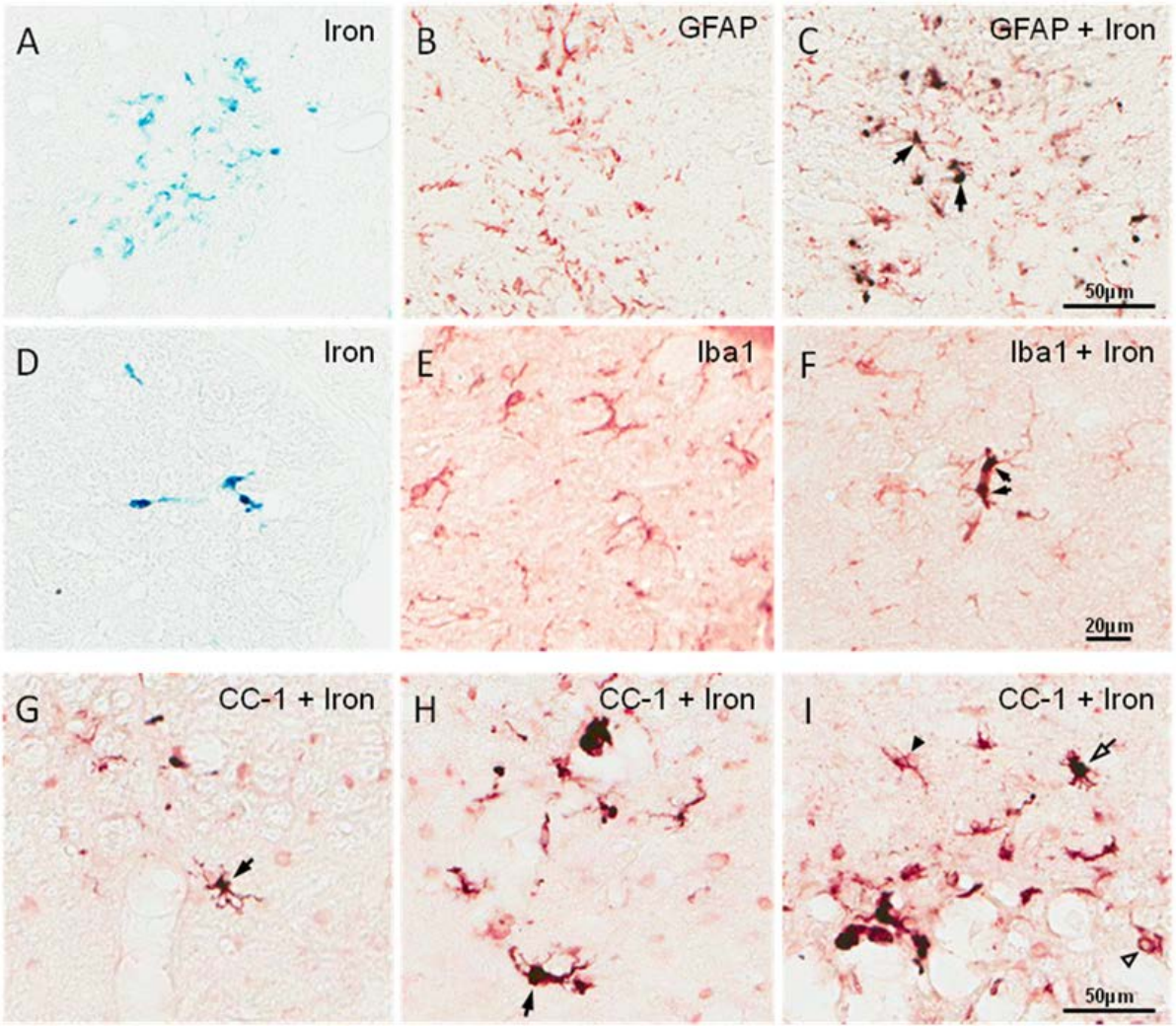

Figure 4. Additional, high-power photomicrographs showing (**A, D**) Prussian Blue stain in relation to (**B**) $GFAP^+$ astrocytes and (**E**) $Iba1^+$ macrophages/microglia in white matter distal to the lesion site at 7 days post-injury. Note that intracellular iron deposits can be observed in both cell types at this time point (arrows in **C** and **F**; blue + red => dark purple / black). (**G-I**) Additional staining for CC-1, a marker for both astrocytes and oligodendrocytes, revealed intracellular iron accumulation in cells reminiscent of both astrocytes (solid arrowhead) and oligodendrocytes (open arrowhead).

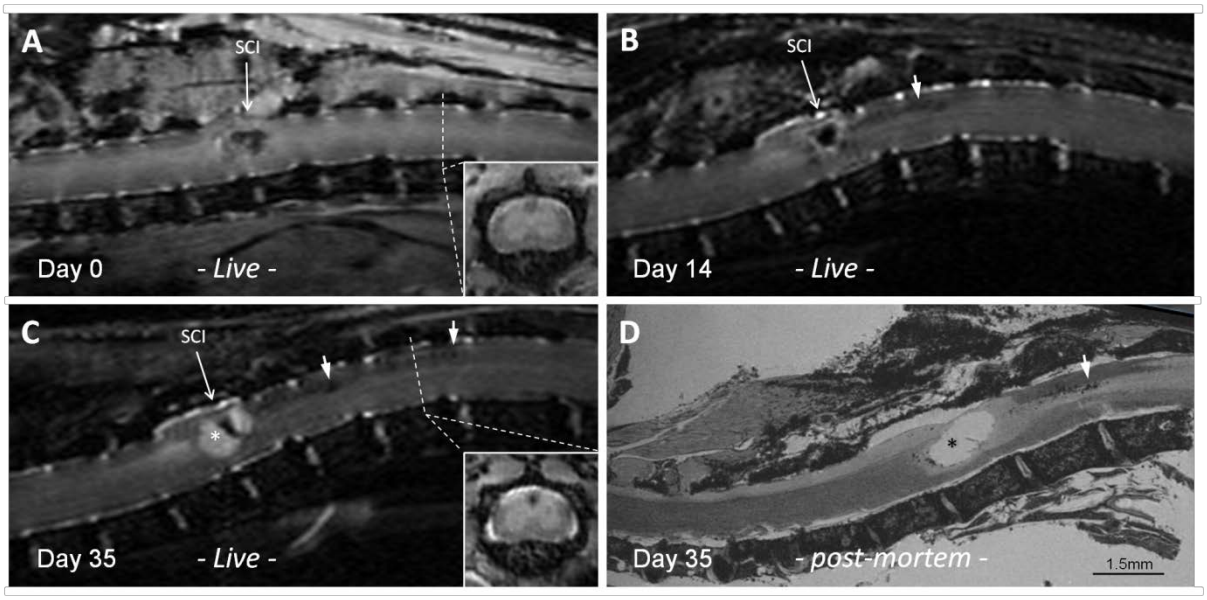

Figure 5. In vivo MR images showing lesion site development and SCI-associated pathology. Iron deposits were detectable in both gradient echo (**A**) FLASH and (**B,C**) spin echo RARE images . Note that (**A**) the hypo-intense signal is restricted to the impact site only at 4 hours after injury. (**B-C**) Progressive loss of signal distal to the lesion site, particularly within the dorsal funiculis, became apparent at day 7 (not shown), 14 and 35 after injury (compare also coronal insets in A and C). Also note the development of a cystic cavity between day 14 and day 35 (asterisk). (**D**) Post-mortem *ex vivo* MR imaging at higher resolution confirmed the presence of hypo-intense regions distal to the injury site (arrow).